

# The Extrasolar Planet $\epsilon$ Eridani b - Orbit and Mass<sup>1</sup>

G. Fritz Benedict<sup>2</sup>, Barbara E. McArthur<sup>2</sup>, George Gatewood<sup>5</sup>, Edmund Nelan<sup>3</sup>, William D. Cochran<sup>2</sup>, Artie Hatzes<sup>4</sup>, Michael Endl<sup>2</sup>, Robert Wittenmyer<sup>2</sup>, Sallie L. Baliunas<sup>6</sup>, Gordon A. H. Walker<sup>7</sup>, Stephenson Yang<sup>7</sup>, Martin Kürster<sup>8</sup>, Sebastian Els<sup>9</sup>, and Diane B. Paulson<sup>10</sup>

## ABSTRACT

*Hubble Space Telescope (HST)* observations of the nearby (3.22 pc), K2 V star  $\epsilon$  Eridani have been combined with ground-based astrometric and radial velocity data to determine the mass of its known companion. We model the astrometric and radial velocity measurements simultaneously to obtain the parallax, proper motion, perturbation period, perturbation inclination, and perturbation size. Because of the long period of the companion,  $\epsilon$  Eri b, we extend our astrometric coverage to a total of 14.94 years (including the three year span of the *HST* data) by including lower-precision ground-based astrometry from the Allegheny Multi-channel Astrometric Photometer. Radial velocities now span 1980.8 – 2006.3. We obtain a perturbation period,  $P = 6.85 \pm 0.03$  yr, semi-major axis  $a = 1.88 \pm 0.20$  mas, and inclination  $i = 30^\circ.1 \pm 3^\circ.8$ . This inclination is consistent with a previously measured dust disk inclination, suggesting coplanarity. Assuming a primary mass  $M_* = 0.83M_\odot$ , we obtain a companion mass  $M = 1.55 \pm 0.24 M_{Jup}$ . Given the relatively young age of  $\epsilon$  Eri ( $\sim 800$  Myr), this accurate exoplanet mass and orbit can usefully inform future direct imaging attempts. We predict the next periastron at 2007.3 with a total separation,  $\rho = 0''.3$  at position angle, p.a. =

---

<sup>2</sup>McDonald Observatory, University of Texas, Austin, TX 78712

<sup>3</sup>Space Telescope Science Institute, 3700 San Martin Dr., Baltimore, MD 21218

<sup>4</sup>Tautenburg Observatory, Germany

<sup>5</sup>Allegheny Observatory, University of Pittsburgh, Pittsburgh, PA

<sup>6</sup>Harvard-Smithsonian Center for Astrophysics, Cambridge, MA 02138

<sup>7</sup>Physics & Astronomy Dept., University of Victoria, BC, V8W 3P6, Canada

<sup>8</sup>Max-Planck-Institut für Astronomie, Königstuhl 17, Heidelberg, D-69117. Germany.

<sup>9</sup>Cerro Tololo Interamerican Observatory, La Serena, Chile.

<sup>10</sup>Goddard Spaceflight Center, Greenbelt, MD 20771.

27°. Orbit orientation and geometry dictate that  $\epsilon$  Eri b will appear brightest in reflected light very nearly at periastron. Radial velocities spanning over 25 years indicate an acceleration consistent with a Jupiter-mass object with a period in excess of 50 years, possibly responsible for one feature of the dust morphology, the inner cavity.

*Subject headings:* astrometry — interferometry — stars: individual ( $\epsilon$  Eri) — stars: radial velocities — stars: late-type — stars: distances — extrasolar planets: masses

## 1. Introduction

$\epsilon$  Eridani ( = HD 22049 = HIP 16537 = HR 1084 = PLX 742), with a spectral type of K2V, is one of the nearest solar-type stars with a distance of about 3.2 pc. It is slightly metal-poor ( $\text{Fe}/\text{H} = -0.13 \pm 0.04$ , Santos *et al.* 2004, Laws *et al.* 2003). Its proximity makes it a prime target for future extrasolar planet direct imaging efforts. The success of these efforts will depend on knowing exactly where to look, requiring accurate orbital elements for the companion. It will depend on the mass of the planetary companion, and will depend on the age of the system. Younger and more massive gas giant planets are predicted to be brighter (Hubbard *et al.* 2002). If young enough, the intrinsic luminosity of  $\epsilon$  Eri b might be greater than its brightness in reflected light. However, planetary mass objects with the age of  $\epsilon$  Eri change intrinsic luminosity by a factor of nearly 100 between  $1 M_{Jup}$  and  $7 M_{Jup}$ . Hence the need for a more precise companion mass.

$\epsilon$  Eri has been the subject of multiple radial velocity (RV) planet searches. Walker *et al.* (1995), using measurements spanning 11 years, found evidence for  $\approx 10$  yr variation with an amplitude of  $15 \text{ m s}^{-1}$ . These results were substantiated by Nelson & Angel (1998) using an analysis of the same data set. Cumming *et al.* (1999) analyzed 11 years of RV data on this star taken at Lick Observatory and found significant variations with comparable amplitude but with a shorter period of 6.9 years. Because of the high level of magnetic activity for  $\epsilon$  Eri (inferred from chromospheric activity), these RV variations were largely interpreted as arising from a stellar activity cycle. The McDonald Observatory Planet Search Program (Cochran & Hatzes 1999) has monitored  $\epsilon$  Eri since late 1988. The

---

<sup>1</sup>Based on observations made with the NASA/ESA Hubble Space Telescope, obtained at the Space Telescope Science Institute, which is operated by the Association of Universities for Research in Astronomy, Inc., under NASA contract NAS5-26555

McDonald results in combination with these other surveys, along with data from ESO (Endl *et al.* 2002), confirmed the presence of long period RV variations and demonstrated that the most likely explanation for the observed RV variations was the presence of a planetary companion with a period,  $P = 6.9$  y. Details of this analysis are given in Hatzes *et al.* (2000).

We obtained three years of astrometry with *HST* with millisecond of arc precision which we combined with radial velocity data as we have in previous planetary mass studies Benedict *et al.* (2002); McArthur *et al.* (2004). Just as in the case of the Hatzes *et al.* (2000) radial velocity analysis, where less-precise data extended the observation span and allowed a companion detection, we anticipated that less-precise astrometry with a 14 year baseline from the Allegheny Multichannel Astrometric Photometer (MAP) astrometry project would improve the astrometric result. Gatewood (2000) reported in a meeting abstract an inclination,  $i = 46^\circ \pm 17^\circ$  and a companion mass  $M_b = 1.2 \pm 0.3 M_{Jup}$  obtained with the MAP data alone. In this study we combine the MAP data with the *HST* data, only to improve the determination of the proper motion of  $\epsilon$  Eri. The parallax and proper motion must be removed as accurately as possible to determine the perturbation orbit of  $\epsilon$  Eri, which, when combined with an estimate of the mass of  $\epsilon$  Eri, will provide the mass of the companion,  $\epsilon$  Eri b.

This paper presents a mass of the planet orbiting  $\epsilon$  Eri discussed in Hatzes *et al.* (2000), not the far longer period object inferred from dust-disk morphology (Quillen & Thorndike 2002). Our mass is derived from combined astrometric and radial velocity data, continuing a series presenting accurate masses of planetary companions to nearby stars. Previous results include the mass of Gl 876b (Benedict *et al.* 2002) and of  $\rho^1$  Cancri d (McArthur *et al.* 2004).

In Section 2 we briefly review the astrometers and discuss the data sets coming from each, and identify our many sources for radial velocities. In Section 3 we present the results of extensive spectrophotometry of the astrometric reference stars, information required to correct relative parallax to absolute. In Section 4 we briefly discuss our astrometric modeling and the quality of our results as determined by residuals. In Section 5 we review our radial velocity data. In Section 6 we derive an absolute parallax and relative proper motion for  $\epsilon$  Eri, those nuisance parameters that must be removed to determine the perturbation orbital parameters. We finally establish the perturbation orbital parameters and, combined with an estimate of the mass of  $\epsilon$  Eri, estimate a mass for  $\epsilon$  Eri b. We discuss system age, dust, and companion detectability in Section 7, and summarize our conclusions in Section 8.

## 2. The Astrometers and Observational Data

### 2.1. *HST* FGS1r

We used *HST* Fine Guidance Sensor 1r (FGS1r) to carry out our space-based astrometric observations. Nelan *et al.* (2003) provides a detailed overview of FGS1r as a science instrument. Benedict *et al.* (2002b) describe the FGS3 instrument’s astrometric capabilities along with the data acquisition and reduction strategies used in the present study. We use FGS1r for the present study because it provides superior fringes from which to obtain target and reference star positions (McArthur *et al.* 2002).

Table 1 presents a log of *HST* FGS observations. Epochs 2–4 contain multiple data sets acquired contiguously, the time span less than a day. Each time is that of the first observation within each epoch. Each distinct observation set typically contains five measurements of  $\epsilon$  Eri. The field was observed at multiple spacecraft roll values, and  $\epsilon$  Eri had to be placed in different, non-central locations within the FGS1r FOV to accommodate the less than optimal distribution of reference stars. FGS photometric sensitivity depends on location within the FOV (*e.g.* Benedict *et al.* 1998) and depends on time, as the FGS PMT age. Given the faintness of our reference stars, we could not use them to provide a high-precision flat field. Hence, we could not extract millimagnitude photometry (*c.f.* Benedict *et al.* 2000a) to monitor  $\epsilon$  Eri stellar activity.

### 2.2. The Allegheny MAP

The Multichannel Astrometric Photometer (MAP) and associated observation and reduction procedures are described by Gatewood (1987). The observational program utilizing the MAP began in 1986, but reluctance to observe at the low  $\epsilon$  Eri declination over the city of Pittsburgh delayed initiation of its observation until January of 1989. Despite the reduced precision and rate of successful observation, the field remained on the MAP program until the installation of new instrumentation early in 2004 (Gatewood 2004).

MAP observations of the brightest stars utilize either a specially filtered 12th channel (*e.g.* Gatewood & Han 2006) or a divide by 16 feature on channel 2, which reduces the count sufficiently for the 16 bit counters. With an R magnitude of 3.0  $\epsilon$  Eri could be placed on channel 2 without counter flooding. The other 10 channels were assigned to the MAP reference stars noted below. An observation consists of 4 x 11 minute sweeps of the ruling across the field with probe rotations and ruling rotations to reduce systematic error (Gatewood 1987). Thus each observation consists of approximately 22 minutes of integration

on each axis. Table 2 presents a log of MAP observations.

### 2.3. Radial Velocities

The radial velocity data used include all data described in Hatzes *et al.* (2000), in addition to more recent data from McDonald Observatory and ESO. These data now span over 25 years. All sources are listed in Table 3. Briefly, McDonald Phases I, II, and III are all data obtained with the 2.7m Smith telescope. The phases correspond (I) to early velocities referenced to atmospheric O<sub>2</sub>, (II) velocities obtained with an I<sub>2</sub> cell, and (III) velocities obtained with the McDonald 2d-Coude spectrograph (Tull *et al.* 1995) and an I<sub>2</sub> cell. The only new radial velocity data included in this new study are from the McDonald Observatory Phase III 2.7m program. They are listed in Table 4. Note that the errors associated with these data are larger than typically produced by this telescope/spectrograph combination (Endl *et al.* 2006) due to high levels of  $\epsilon$  Eri stellar activity.

## 3. $\epsilon$ Eri Astrometric Reference Frames

Any prior knowledge concerning the fifteen stars included in our reference frame eventually enters our modeling as observations with error, and yields the most accurate parallax and proper motion for the prime target,  $\epsilon$  Eri. These periodic and non-periodic motions must be removed as accurately and precisely as possible to obtain the perturbation inclination and size caused by  $\epsilon$  Eri b.

### 3.1. The MAP Reference Frame

Figure 1 shows the distribution of the ten reference stars in the 130 MAP  $\epsilon$  Eri observation sets (Table 2). Note that the areal coverage is approximately  $0^{\circ}6 \times 0^{\circ}6$ , allowing for the use of relatively bright reference stars, well-distributed around the prime target  $\epsilon$  Eri, in contrast to the case for the *HST* FGS (below).

### 3.2. The FGS Reference Frame

Figure 2 shows the distribution in FGS1r pickle coordinates of the 52 sets of five reference star measurements for the  $\epsilon$  Eri field. The arcing pattern is enforced by the requirement that

*HST* must roll to keep its solar panels fully illuminated throughout the year. To ensure access to all reference stars for every observation set, it was not possible to keep  $\epsilon$  Eri (symbol,  $\times$ ) located in the center of the FGS1r FOV. At each epoch we measured each reference stars 2 – 4 times, and  $\epsilon$  Eri 4–5 times.

### 3.3. Absolute Parallaxes for the Reference Stars

Because the parallax determined for  $\epsilon$  Eri is measured with respect to reference frame stars which have their own parallaxes, we must either apply a statistically- derived correction from relative to absolute parallax (van Altena Lee & Hoffleit 1995, Yale Parallax Catalog, YPC95), or estimate the absolute parallaxes of the reference frame stars. In principle, the colors, spectral type, and luminosity class of a star can be used to estimate the absolute magnitude,  $M_V$ , and  $V$ -band absorption,  $A_V$ . The absolute parallax is then simply,

$$\pi_{\text{abs}} = 10^{-(V-M_V+5-A_V)/5} \quad (1)$$

#### 3.3.1. Reference Star Photometry

Our bandpasses for reference star photometry include:  $V$  (from FGS1r), and  $JHK$  from 2MASS<sup>2</sup>. The  $JHK$  values have been transformed to the Bessell & Brett (1988) system using the transformations provided in Carpenter (2001). Table 6 lists  $VJHK$  photometry for the target and reference stars indicated in Figures 1 and 2. Figure 3 contains a  $(J - K)$  vs.  $(V - K)$  color-color diagram with reference stars and  $\epsilon$  Eri labeled. Schlegel *et al.* (1998) find an upper limit  $A_V \sim 0.1$  towards  $\epsilon$  Eri. In the following we adopt  $\langle A_V \rangle = 0.0$ , but increase the error on reference star distance moduli by 0.1 magnitudes to account for absorption uncertainty.

The derived absolute magnitudes are critically dependent on the assumed stellar luminosity, a parameter impossible to obtain for all but the latest type stars using only Figure 3. To confirm the luminosity classes we obtain UCAC2 proper motions (Zacharias *et al.* 2004) for a one-degree-square field centered on  $\epsilon$  Eri, and then iteratively employ the technique of reduced proper motion (Yong & Lambert 2003; Gould & Morgan 2003) to discriminate between giants and dwarfs. The end result of this process is contained in Figure 4.

---

<sup>2</sup>The Two Micron All Sky Survey is a joint project of the University of Massachusetts and the Infrared Processing and Analysis Center/California Institute of Technology

### 3.3.2. Adopted Reference Frame Absolute Parallaxes

We derive absolute parallaxes using our estimated spectral types and luminosity class and  $M_V$  values from Cox (2000). Our adopted input errors for distance moduli,  $(m - M)_0$ , are 0.4 mag for all reference stars (except ref-2 and -6, as discussed below). Contributions to the error are a small but undetermined  $A_V$  and errors in  $M_V$  due to uncertainties in color to spectral type mapping. We estimate a spectral type for reference star ref-6 only through its apparent magnitude, hence, the larger error in its distance modulus. Ref-2, which in Figure 3 straddles the gap between giants and dwarfs, was finally typed K4V, because the  $\chi^2$  (from modeling of the reference frame) significantly decreased, using that typing. Its input parallax error was also increased. All reference star absolute parallax estimates are listed in Table 7. Individually, no reference star absolute parallax is better determined than  $\frac{\sigma_\pi}{\pi} = 18\%$ . The average input absolute parallax for the reference frame is  $\langle \pi_{abs} \rangle = 4.9$  mas, a quantity known to  $\sim 5\%$  (standard deviation of the mean of fifteen reference stars). We compare this to the correction to absolute parallax discussed and presented in YPC95 (Sec. 3.2, Fig. 2). Entering YPC95, Fig. 2, with the Galactic latitude of  $\epsilon$  Eri,  $b = -48^\circ$ , and average magnitude for the reference frame,  $\langle V_{ref} \rangle = 12.2$ , we obtain a correction to absolute of 2.3 mas, considerably different. Rather than apply a model-dependent correction to absolute parallax, we introduce our spectrophotometrically-estimated reference star parallaxes into our reduction model as observations with error.

## 4. The Astrometric Model

The  $\epsilon$  Eri reference frame contains fifteen stars and has been measured by two different astrometers, FGS1r and MAP. The only object in common is  $\epsilon$  Eri. From these positional measurements we determine the scale, rotation, and offset “plate constants” relative to an arbitrarily adopted constraint epoch for each observation set. As for all our previous astrometric analyses, we employ GaussFit (Jefferys *et al.* 1988) to minimize  $\chi^2$ . The solved equations of condition for the  $\epsilon$  Eri field are:

$$x' = x + lcx(B - V) - \Delta XFx \quad (2)$$

$$y' = y + lcy(B - V) - \Delta XFy \quad (3)$$

$$\xi = Ax' + By' + C - \mu_\alpha \Delta t - P_\alpha \pi \quad (4)$$

$$\eta = Dx' + Ey' + F - \mu_\delta \Delta t - P_\delta \pi \quad (5)$$

for FGS1r data and

$$\xi = Ax + By + C - P_\alpha \pi - \mu_\alpha \Delta t \quad (6)$$

$$\eta = Dx + Ey + F - P_\delta\pi - \mu_\delta\Delta t \quad (7)$$

for the MAP data. Identifying terms,  $x$  and  $y$  are the measured coordinates from *HST* and the MAP;  $(B - V)$  represents the  $(B - V)$  color of each star, estimated from its spectral type,  $A_V$ , and  $(J - K)$  color listed in Table 6; and  $l_cx$  and  $l_cy$  are the lateral color corrections, applied only to FGS1r data. Here  $\Delta X_Fx$  and  $\Delta X_Fy$  are the cross filter corrections in  $x$  and  $y$ , applied to the observations of  $\epsilon$  Eri in FGS1r.  $A$ ,  $B$ ,  $D$  and  $E$  are scale- and rotation plate constants,  $C$  and  $F$  are offsets;  $\mu_\alpha$  and  $\mu_\delta$  are proper motions;  $\Delta t$  is the epoch difference from the mean epoch;  $P_\alpha$  and  $P_\delta$  are parallax factors; and  $\pi$  is the parallax. We obtain the parallax factors from a JPL Earth orbit predictor (Standish 1990), upgraded to version DE405. Orientation to the sky for the FGS1r data is obtained from ground-based astrometry (2MASS Catalog) with uncertainties of 0.01.

#### 4.1. Assessing Reference Frame Residuals

Histograms of the MAP residuals (Figure 5) indicate per-observation precision of  $\sim 7$  mas. Because we are seeking the signature of a perturbation over three times smaller than that per-observation precision, the MAP data were only used to lower the errors on parallax and proper motion, not to establish any perturbation parameters. As for the FGS data, the Optical Field Angle Distortion calibration McArthur *et al.* (2002) reduces as-built *HST* telescope and FGS1r distortions with magnitude  $\sim 1''$  to below 2 mas over much of the FGS1r field of regard. From histograms of the FGS astrometric residuals (Figure 6) we conclude that we have obtained correction at the  $\sim 1$  mas level. The reference frame 'catalogs' for MAP and FGS1r in  $\xi$  and  $\eta$  standard coordinates (Table 8) were determined with  $\langle \sigma_\xi \rangle = 1.0$  and  $\langle \sigma_\eta \rangle = 1.3$  mas (MAP), and  $\langle \sigma_\xi \rangle = 0.3$  and  $\langle \sigma_\eta \rangle = 0.2$  mas (FGS).

### 5. Radial Velocities

Measurements from four planet search groups were included in our modeling. Table 3 lists the source, coverage, technique, number of observations and the rms deviation from the final orbit of these observations. The weighting of the RV data was carefully evaluated with independent modeling and significant outliers were filtered. For example - if five data points were taken in succession, all assigned with the same weight and one point was 50 m s<sup>-1</sup> offset from the others, that point was discarded for this solution. Initially these points were merely re-weighted, but later discarded as spurious data. The total number of observations so discarded was less than 1% of the aggregate data. This improved our goodness of fit ( $\chi^2$  /degrees of freedom) measurement of the modelling for the RV data set

from 0.94 in the announcement paper to 0.30 in the current analysis.

## 6. $\epsilon$ Eri Parallax, Proper Motion, and Perturbation Orbit from Astrometry and Radial Velocities

Solving for relative parallax, proper motion, and orbital motion, using astrometry and radial velocities simultaneously, the model now becomes,

$$\xi = aX + bY + c - P_x * \pi - \mu_x * t - ORBIT_x \quad (8)$$

$$\eta = -bX + aY + f - P_y * \pi - \mu_y * t - ORBIT_y \quad (9)$$

where ORBIT is a function (through Thiele-Innes constants) of the traditional astrometric and radial velocity orbital elements listed in Table 11.

The period (P), the epoch of passage through periastron in years (T), the eccentricity (e) and the angle in the plane of the true orbit between the line of nodes and the major axis ( $\omega$ ), are constrained to be equal for the radial velocity and astrometry portions of the model. Only radial velocity provides information with which to determine the half-amplitudes ( $K_1$ ) and  $\gamma$ , the systemic velocity. Combining radial velocity observations from different sources is possible with GaussFit, which has the ability to simultaneously solve for many separate velocity offsets (because velocities from different sources are relative, having differing zero points), along with the other orbital parameters.

We force a relationship between the astrometry and the radial velocity by a constraint from Pourbaix & Jorissen (2000)

$$\frac{\alpha_A \sin i}{\pi_{abs}} = \frac{PK_1(1 - e^2)^{1/2}}{2\pi \times 4.7405} \quad (10)$$

where quantities derived only from astrometry (parallax,  $\pi_{abs}$ , primary perturbation orbit size,  $\alpha_A$ , and inclination,  $i$ ) are on the left, and quantities derivable from both (the period,  $P$  and eccentricity,  $e$ ), or radial velocities only (the radial velocity amplitude for the primary,  $K_1$ ), are on the right.

Combining RV measurements complete through 2006.3 (Table 3), all the astrometric measurements, and the Equation 10 constraint, we solve for parallax, proper motion, and the semi-major axis, orbit orientation, and orbit inclination for the perturbation caused by the companion. For the parameters critical in determining the mass of  $\epsilon$  Eri we find a parallax,  $\pi_{abs} = 311.37 \pm 0.10$  mas and a proper motion  $976.54 \pm 0.1$  mas  $y^{-1}$  in position

angle  $269^{\circ}0 \pm 0^{\circ}.6$ . Table 10 compares values for the parallax and proper motion of  $\epsilon$  Eri from *HST* and *HIPPARCOS*. We note satisfactory agreement. Our precision and extended study duration have significantly improved the accuracy and precision of the parallax and proper motion of  $\epsilon$  Eri.

At this stage we can assess the reality of any  $\epsilon$  Eri perturbation by plotting residuals to a model that does not include an orbit. Figure 7 shows the X and Y components of only the higher-precision astrometry FGS residuals plotted as grey dots. The lower precision MAP data were not considered in the determination of the orbital parameters. We also plot normal points formed from those dots at nine epochs. Finally, each plot contains as a dashed line the X and Y components of the perturbation we find by including an orbit in our modeling.

We find a perturbation size,  $\alpha_A = 1.88 \pm 0.19$  mas, and an inclination,  $i = 30^{\circ}.1 \pm 3^{\circ}.8$ . These, and the other orbital elements for the perturbation, are listed in Table 11 with  $1-\sigma$  errors. Errors generated by GaussFit (Jefferys *et al.* 1988) come from a maximum likelihood estimation that is an approximation to a Bayesian maximum a posteriori estimator with a flat prior (Jefferys 1990). Figure 8 illustrates the Pourbaix and Jorissen relation (Equation 10) between parameters obtained from astrometry (left-side) and radial velocities (right side) and our final estimates for  $\alpha_A$  and  $i$ . As seen in Tables 10 and 11, most of the errors of the terms in Equation 10 are quite small. In essence, our simultaneous solution uses the Figure 8 curve as a quasi-Bayesian prior, sliding along it until the astrometric and radial velocity residuals are minimized. Gross deviations from the curve are minimized by the high precision of many of the terms in Equation 10. Figure 9 contains all radial velocity measures and the predicted velocity curve from the simultaneous solution. Compared to the typical perturbation radial velocity curve (e.g. Hatzes *et al.* 2005, McArthur *et al.* 2004, Cochran *et al.* 2004), Figure 9 exhibits far more scatter about the derived orbit. There are two reasons for this. The perturbation amplitude is small ( $K_1 = 18.5 \text{ m s}^{-1}$ ), and  $\epsilon$  Eri is an active star, as discussed in Hatzes *et al.* (2000). Reiterating their conclusions, none of the activity cycles have periods commensurate with the planetary perturbation period. Figure 10 presents the astrometric residuals and the derived perturbation orbit for the primary star,  $\epsilon$  Eri. Stellar activity has even less of an effect on astrometry at our level of precision. A star spot covering 30% of the surface would induce a photocenter shift of less than 0.2 mas (Sozzetti 2005). The astrometry confirms the existence of the companion.

Our analysis of the radial velocities (now spanning over 25 years, all shown in Figure 9) included a linear drift term, a change in velocity as a function of time. This drift is clearly seen in the overplotted final radial velocity curve, and amounts to  $0.32 \pm 0.05 \text{ m s}^{-1} \text{ yr}^{-1}$ . Such a change can be caused by longer-period companions and/or secular acceleration (Kürster & Endl 2004). The secular acceleration expected for  $\epsilon$  Eri is (van de Kamp,

1967) quite small,  $0.07 \text{ m s}^{-1} \text{ yr}^{-1}$ . The trend we find is over four times larger than the predicted secular acceleration, and is approximately the acceleration one might find for a planet similar in mass to  $\epsilon$  Eri b, but with a 50–100 year period. Figure 9 shows sufficient enough overlap among the many velocity data sets that the trend is unlikely an artifact due to a mismatch in the center of mass velocity offsets (discussed above) obtained for each set. Typical offset random error is  $\sim 1 \text{ m s}^{-1}$ . While this acceleration is not a detection of the longer-period companion ( $40 < a < 60 \text{ AU}$ ) invoked by Quillan & Thorndike (2002) and Ozernoy *et al.* (2000) to modify the dust distribution as discussed below in Section 7, it may (with a semimajor axis 10–20 AU) be at least partially responsible for the inner cavity in the dust disk distribution imaged by Greaves *et al.* (2005). The astrometric motion over 15 years due to this possible tertiary would be of order 3 mas and difficult to separate from proper motion, e.g., Black & Scargle (1982).

The planetary mass depends on the mass of the primary star, for which we have adopted  $M_* = 0.83 \pm 0.05 M_\odot$  (Di Folco *et al.* 2004). For this  $M_*$  we find  $M_b = 1.55 \pm 0.24 M_{Jup}$ . The companion is clearly an extrasolar giant planet. In Table 12 the mass value,  $M_b$ , incorporates the present uncertainty in  $M_*$ . Until  $\epsilon$  Eri b is directly detected, its radius is unknown. From a review of exoplanet masses and radii (Guillot 2005), a radius of  $R = 1 R_{Jup}$  seems reasonable.

Our eccentricity value,  $e = 0.70$ , allows for a significant difference in separation between star and exoplanet at apastron compared to periastron. At time of periastron passage,  $T_0 = 2007.29$ , we predict a separation  $0''.3 \pm 0''.1$  at a position angle of  $27^\circ$ . At the next apastron, to occur 2010.71, the separation should be  $1''.8 \pm 0''.4$  at position angle of  $207^\circ$ . The dominant sources of error for the separations are the eccentricity (6%) and the  $\epsilon$  Eri b planet mass (15%).

## 7. Discussion

Our accurate mass and orbital parameters for this planetary companion have value for future direct imaging projects. We now know where near  $\epsilon$  Eri to look for  $\epsilon$  Eri b. We would now like to know when to look, what bandpass is best, and what we can expect to see. As stated previously system age, companion mass, and orbital geometry are critical parameters when estimating visibility.

A high level of chromospheric activity is seen for  $\epsilon$  Eri (e.g. Gray & Baliunas 1995), and is consistent with a relatively young age;  $< 1 \text{ Gyr}$  (Soderblom & Däppen 1989). Saffe *et al.* (2005) used the calibrations of Donahue (1993) and Rocha-Pinto & Maciel (1998)

(which corrected the age with an effect from stellar metallicity) to estimate ages of 0.66 and 0.82 Gyr, respectively. Henry (1986) derived from CaII lines a value of 0.8 Gyr. Song *et al.* (2000) used Li abundances with its position in the H-R diagram and kinematics to derive a value of  $0.73 \pm 0.2$  Gyr. Di Folco *et al.* (2004) estimated the age at 0.85 Gyr, a value obtained through the measurement of the radius of  $\epsilon$  Eri by long-baseline interferometry. Their modeling is consistent with a primary mass of  $M_* = 0.83 \pm 0.05 M_\odot$ , an estimate that weakly depends on measured metallicity, which ranges  $-0.13 < [\text{Fe}/\text{H}] < -0.06$  in the literature.

Hubbard *et al.* (2002) predict the intrinsic luminosity of extrasolar giant planets as a function of mass and age. From their Figure 11, an age of 800 My Di Folco *et al.* (2004), and our planetary mass,  $M_b = 1.55 \pm 0.24 M_{Jup}$ , we find for  $\epsilon$  Eri b,  $L/L_\odot = 1.6 \times 10^{-8}$ . Using the Di Folco *et al.* (2004)  $T_{eff} = 5135$  K, their radius,  $R_* = 0.743 R_\odot$ , our parallax,  $\pi_{abs} = 311.37$  mas, and a bolometric correction, B.C. = -0.27, from Flower (1996), we find a difference in bolometric magnitude of  $\epsilon$  Eri compared to the Sun of  $\Delta M_{bol} = +1.17$ . Hence, neglecting reflected light and orbital phase,  $\epsilon$  Eri b is  $4.67 \times 10^{-8}$  fainter in bolometric luminosity than  $\epsilon$  Eri.

Sudarsky *et al.* (2005), Dyudina *et al.* (2005), and Burrows *et al.* (2004) discuss exoplanet apparent brightness in reflected host star light as functions of orbit geometry, orbital phase, and cloud cover. Burrows *et al.* (2004) predict the full spectrum of  $\epsilon$  Eri b from 0.5 to  $6 \mu\text{m}$ , asserting that the planet is too young for its atmosphere to contain condensed ammonia clouds. However,  $\epsilon$  Eri b should exhibit  $\text{H}_2\text{O}$  clouds. They predict a maximum planet/host star flux ratio,  $\log_{10}(F_{planet}/F_{star}) \sim -7$ , at  $\sim 4.5 \mu\text{m}$  with a secondary peak,  $\log_{10}(F_{planet}/F_{star}) \sim -8$ , at  $\sim 1 \mu\text{m}$ . Dyudina *et al.* (2005) predict that for  $\omega = 30^\circ$ , inclination,  $i = 30^\circ$ ,  $e = 0.5$ , and a Jupiter-like atmosphere, the planet/host star flux ratio is largest very shortly after periastron, late 2007. However, the separation remains small ( $\sim 0''.3$ ). The inclination of the  $\epsilon$  Eri system,  $i = 30^\circ$ , is likely to decrease the flux ratio by approximately a factor of two (Sudarsky *et al.* 2005), compared to a  $i = 90^\circ$  edge-on orientation. Given the orientation of the orbit of  $\epsilon$  Eri b (its ascending node,  $\Omega' = 254^\circ$ ), the disk of  $\epsilon$  Eri b is most fully illuminated at apastron, but is three times further away from its primary.

The dusty rings or debris disks surrounding  $\epsilon$  Eri also suggest relative youth for the system. Photometric measurements from the IRAS satellite (Aumann, 1988) provided the first hint of dust around  $\epsilon$  Eri. Subsequently, Submillimeter Common-User Bolometric Array (SCUBA) measurements were made between 1997 and 2002. These measurements determined that the dust, distributed in a ring, is located 65 AU from the star (Greaves *et al.* 1998, 2005). The sub-mm bolometer, SIMBA, provided observational confirmation of this extended dust disk (Schutz *et al.* 2004). The STIS CCD camera on *HST* took deep optical images

around  $\epsilon$  Eri in an effort to find an optical counterpart for the sub-millimeter observations. These measurements did not provide clear evidence for the detection of that optical counterpart, but did place a limit on the optical surface brightness of the dust, that it could not be brighter than approximately  $25 \text{ STMAG arcsec}^{-2}$ , which places constraints on the nature and amount of the smallest dust grains (Proffitt *et al.* 2004).

Observational and theoretical searches for the signature of planetary/brown dwarf objects in the structure of the dust disk around  $\epsilon$  Eri are underway. Clumps seen in the ring are thought to come from the interaction between the disk and a massive planetary body (Holland *et al.* 2003). Adaptive optics on the Keck Telescope were used to search for extrasolar planets. These studies found no evidence of brown dwarf or planetary companions down to 5 Jupiter masses at the angular separations comparable to that of the dust rings (Macintosh *et al.* 2003). Spitzer Space Telescope (SST) observations made with the Multi-band Imaging Photometer (MIPS) and the InfrRed Spectrograph (IRS) have confirmed the disk and provided evidence for asymmetries in the structure of the disk that may have been caused by the gravitational perturbation of sub-stellar companions (Marengo *et al.* 2004).

Two recent studies suggested that debris disks and long-period planets co-exist, with planetary bodies ‘sculpting’ the disk.  $\epsilon$  Eri is the prototypical system. First, high-resolution modeling of the structure of the disk around  $\epsilon$  Eri predict an angular motion of the asymmetry of the disk of about  $0.6\text{--}0.8 \text{ yr}^{-1}$  (Ozernoy *et al.* 2000). Secondly, Quillen & Thorndike (2002) carried out numerical simulations of dust particles captured in mean motions resonances with a hypothetical planet ( $e = 0.3$ ,  $M = 10^{-4} M_{\odot}$ ,  $a = 40 \text{ AU}$ ) at periastron. These produced a dust distribution that agreed with the morphology of the dust ring around  $\epsilon$  Eri presented by Greaves *et al.* (1998, 2005). An investigation into the dynamics of the dust ring around  $\epsilon$  Eri (Moran, Kuchner & Holman, 2004) concluded that the eccentricity of the dust released in the inner ring ( $<20 \text{ AU}$ ) could reveal patterns in the dust which could confirm the existence of the planet reported by Hatzes *et al.* (2000).

We determined an inclination of  $i=30.1 \pm 3.2$  for  $\epsilon$  Eri b. Our measured inclination is consistent with the previously measured dust disk inclination from 450 and 850  $\mu\text{m}$  maps of Greaves *et al.* (1998, 2005),  $i = 25^{\circ}$ . This suggests that the dust disk and plane of the orbit of  $\epsilon$  Eri b are coincident and that the dust distribution is nearly circular. This provides support for hierarchical accretion models for planet formation Pollack *et al.* (1996), where coplanar dust and a debris disk are expected remnants of planet formation (Tsiganis *et al.* 2005). Lastly,  $\epsilon$  Eri b and the possible tertiary deduced from the linear trend in the radial velocities (Section 6) would most likely eject particles that would spiral inward, and recent SCUBA submillimeter observations have shown that the center of the disk is relatively excavated of dust, with half or less of the signals seen in the ring (Greaves *et al.* 2005).

## 8. Conclusions

Analyzing three years of *HST* FGS and over 14 years of Allegheny Observatory MAP astrometry, we find an independently determined parallax and proper motion for  $\epsilon$  Eri that agree within the errors with HIPPARCOS.

Astrometric observations with *HST* FGS, combined with long-duration Allegheny MAP astrometry and ground based radial velocities, have confirmed the existence of the planet orbiting  $\epsilon$  Eri, first suggested by Walker *et al.* (1995), noted by Cummings *et al.* (1999), and finally announced by Hatzes *et al.* (2000).

Combining the astrometry with radial velocities from six different sources, spanning 25 years, and applying the Pourbaix & Jorissen constraint between astrometry and radial velocities, we obtain for the perturbing object  $\epsilon$  Eri b a period,  $P=6.85 \pm 0.02$  y, inclination,  $i=30.1 \pm 3.2$ , and perturbation semimajor axis,  $\alpha_A = 1.88 \pm 0.19$  mas. Assuming for  $\epsilon$  Eri a stellar mass  $M_* = 0.83 \pm 0.05 M_\odot$ , we obtain a mass for  $\epsilon$  Eri b,  $M_b = 1.55 \pm 0.24 M_{Jup}$ . This companion inclination matches the disk inclination determined by Greaves *et al.* (2005).

Our astrometry predicts for  $\epsilon$  Eri b periastron passage at  $T_0 = 2007.29$ , with a separation  $\sim 0''.3$  in position angle  $27^\circ$  ( $a = 3.39$  AU). At the next apastron, to occur 2010.71, the separation should be  $1''.7$  in position angle  $207^\circ$ . The orbital geometry suggests that 2007.97 (late December 2007) is the most favorable time for direct detection in reflected light. For an  $\epsilon$  Eri age  $\sim 850$  My and our determined mass,  $\epsilon$  Eri b will have an intrinsic luminosity  $L/L_\odot = 1.6 \times 10^{-8}$ ,  $4.67 \times 10^{-8}$  times fainter in bolometric luminosity than  $\epsilon$  Eri.

Radial velocities spanning 25 years indicate a long-term linear trend, an acceleration consistent with a Jupiter-mass object with a period of 50–100 years. This is a possible detection of a tertiary companion responsible for a major feature of the dust morphology, the central cavity.

Support for this work was provided by NASA through grants GO-09167, GO-09347, and GO-09969 from the Space Telescope Science Institute, which is operated by the Association of Universities for Research in Astronomy, Inc., under NASA contract NAS5-26555. The Allegheny Observatory received support from the National Science Foundation through grant AST-0098552 and the National Aeronautics and Space Administration through grant NAG-510628. This publication makes use of data products from the Two Micron All Sky Survey, which is a joint project of the University of Massachusetts and the Infrared Processing and Analysis Center/California Institute of Technology, funded by NASA and the NSF. This research has made use of the SIMBAD database, operated at CDS, Strasbourg, France; the NASA/IPAC Extragalactic Database (NED) which is operated by JPL, Cali-

ifornia Institute of Technology, under contract with the NASA; and NASA's Astrophysics Data System Abstract Service. We thank an anonymous referee for a careful review and constructive criticism which improved this final version of the paper.

## REFERENCES

- Aumann, H. H., 1998, *AJ*, 96, 1415
- Benedict, G. F., *et al.* 2002, *ApJ*, 581, L115
- Benedict, G. F., *et al.* 2000a, *AJ*, 119, 2382
- Benedict, G. F., McArthur, B. E., Franz, O. G., Wasserman, L. H., & Henry, T. J. 2000b, *AJ*, 120, 1106
- Benedict, G. F., *et al.* . 1998, *AJ*, 116, 429
- Bessell, M. S. & Brett, J. M. 1988, *PASP*, 100, 1134
- Black, D. C. & Scargle, J. D. 1982, *ApJ*, 263, 854
- Burrows, A., Sudarsky, D., & Hubeny, I. 2004, *ApJ*, 609, 407
- Carpenter, J. M. 2001, *AJ*, 121, 2851
- Ciardi, D., 2004, private communication
- Cochran, W. D., & Hatzes, A. P. 1999, *ASP Conf. Ser.* 185: IAU Colloq. 170: Precise Stellar Radial Velocities, 185, 113
- Cochran, W. D., *et al.* 2004, *ApJ*, 611, L133
- Cox, A. N. 2000, *Allen's Astrophysical Quantities*, 4th ed. Publisher: New York: AIP Press, Springer, 2000. Edited by Arthur N. Cox.
- Cumming, A., Marcy, G. W., & Butler, R. P. 1999, *ApJ*, 526, 890
- Di Folco, E., Thévenin, F., Kervella, P., Domiciano de Souza, A., Coudé du Foresto, V., Ségransan, D., & Morel, P. 2004, *A&A*, 426, 601
- Donahue, R. A., 1993, Ph D Thesis, New Mexico State University
- Dyudina, U. A., Sackett, P. D., Bayliss, D. D. R., Seager, S., Porco, C. C., Throop, H. B., & Dones, L. 2005, *ApJ*, 618, 973
- Endl, M., Cochran, W. D., Wittenmyer, R. A., & Hatzes, A. P. 2006, *AJ*, 131, 3131
- Endl, M., Kürster, M., Els, S. H. A. P., Cochran, W. D., Dennerl, K., Döbereiner, S. 2002, *A&A*, 392, 671

- Flower, P. J. 1996, ApJ, 469, 355
- Gray, D.F. & Baliunas, S.L. 1995, ApJ, 441, 442
- Gatewood, G. and Han, I., 2006, AJ 131, 1015
- Gatewood, G., 2004, BAAS, 36, 4.10
- Gatewood, G. 2000, BAAS, 32, 1051
- Gatewood, G. D. 1987, AJ, 94, 213
- Greaves, J. S., et al. 2005, ApJ, 619, L187
- Greaves, J. S., et al. 1998, ApJ, 506, L133
- Gould, A. & Morgan, C. W. 2003, ApJ, 585, 1056
- Guillot, T. 2005, Annual Review of Earth and Planetary Sciences, 33, 493
- Hatzes, A. P. *et al.* 2000, ApJ, 544, L145
- Hatzes, A. P., Guenther, E. W., Endl, M., Cochran, W. D., Döllinger, M. P., & Bedalov, A. 2005, A&A, 437, 743
- Henry, T.J., *et al.* 1996, AJ, 111, 439
- Holland, W. S., *et al.* 2003, ApJ, 582, 1141
- Hubbard, W. B., Burrows, A., & Lunine, J. I. 2002, ARA&Ap, 40, 103
- Jefferys, W. H. 1990, Biometrika, 77, 597
- Jefferys, W., Fitzpatrick, J., & McArthur, B. 1988, Celest. Mech. 41, 39.
- Kürster, M., & Endl, M. 2004, ASP Conf. Ser. 321: Extrasolar Planets: Today and Tomorrow, 321, 84
- Laws, C., et al. 2003, AJ, 125, 2664
- Macintosh, B., et al. 2003, ApJ, 594, 538.
- Marengo, M., et al. 2004, BAAS, 205, 1125.
- McArthur, B., Benedict, G. F., Jefferys, W. H., & Nelan, E. 2002, The 2002 HST Calibration Workshop. Edited by Santiago Arribas, Anton Koekemoer, and Brad Whitmore. Baltimore, MD: Space Telescope Science Institute, p 373

- McArthur, B. E., *et al.* 2004, ApJ, 614, L81
- Moran, S. M., Kuchner, M. J., & Holman, M. J. 2004, ApJ, 612, 1163
- Nelan, E., *et al.*, “Fine Guidance Sensor Instrument Handbook,” version 12.0, Baltimore, STScI
- Nelson, A. F., & Angel, J. R. P. 1998, ApJ, 500, 940
- Ozernoy, L. M., *et al.* , 2000, ApJ, 537, L147
- Pollack, J. B., Hubickyj, O., Bodenheimer, P., Lissauer, J. J., & Greenzweig, Y. 1996, Icarus, 124, 62
- Pourbaix, D. & Jorissen, A., 2000, A&AS, 145, 161
- Proffitt, C. R., *et al.* , 2004 AJ612, 481
- Quillen, A. C., & Thorndike, S., 2002, ApJ578, L149
- Rocha-Pinto, H., & Macile, W. 1998, MNRAS, 298, 161
- Saffee, C., Gomez, M., & Chavero, C., 2005, astro-ph archive 0510092, submitted to A&A
- Santos, N. C., Israelian, G., & Mayor, M. 2004, A&A, 415, 1153
- Schlegel, D. J., Finkbeiner, D. P., & Davis, M. 1998, ApJ, 500, 525
- Schutz, O., *et al.* 2004, A&A, 414, L9
- Soderblom, D.R., & Däppen, W. 1989, ApJ, 375, 722.
- Sozzetti, A. 2005, PASP, 117, 1021
- Song, I., *et al.* 2000 ApJ, 533, L41. 1989, ApJ, 375, 722.
- Standish, E. M. J. 1990, A&A, 233, 252
- Sudarsky, D., Burrows, A., Hubeny, I., & Li, A. 2005, ApJ, 627, 520
- Tsignas, K., *et al.* , 2005, Nature, 435, 459
- Tull, R. G., MacQueen, P. J., Sneden, C., & Lambert, D. L. 1995, PASP, 107, 251
- van Altena, W. F., Lee, J. T., & Hoffleit, E. D. 1995, Yale Parallax Catalog (4th ed. ; New Haven, CT: Yale Univ. Obs.) (YPC95)

van de Kamp, P. 1967, *Principles of Astrometry*, San Francisco, CA: W. H. Freeman and Company

Walker, G. A. H., Walker, A. R., Irwin, A. W., Larson, A. M., Yang, S. L. S., & Richardson, D. C. 1995, *Icarus*, 116, 359

Yong, D. & Lambert, D. L. 2003, *PASP*, 115, 796

Zacharias, N. *et al.* 2004, *AJ*, 127, 3043

Table 1. Log of  $\epsilon$  Eri FGS Observations

Epoch	MJD <sup>a</sup>	Year	Roll (°) <sup>b</sup>	Epoch	MJD	Year	Roll (°)
1	51946.528	2001.101	96.9	24	52862.76878	2003.609	281.0
2	51982.209	2001.198	91.0	25	52865.68038	2003.617	280.0
3	52180.393	2001.741	280.0	26	52868.70565	2003.625	280.0
4	52309.062	2002.093	97.0	27	52871.75072	2003.634	280.0
5	52497.787	2002.610	280.0	28	52874.84206	2003.642	280.0
6	52500.124	2002.616	280.0	29	53007.24013	2004.005	106.0
7	52503.062	2002.624	280.0	30	53010.26367	2004.013	105.0
8	52506.667	2002.634	280.0	31	53014.10664	2004.024	105.0
9	52509.629	2002.642	280.0	32	52672.409	2003.088	105.0
10	52513.545	2002.653	280.0	33	52679.324	2003.107	105.0
11	52537.069	2002.718	280.0	34	52681.993	2003.114	105.0
12	52540.651	2002.727	280.0	35	52682.004	2003.114	105.0
13	52543.679	2002.736	280.0	36	52683.127	2003.117	105.0
14	52642.962	2003.007	105.0	37	52686.352	2003.126	105.0
15	52645.364	2003.014	105.0	38	52688.330	2003.132	105.0
16	52649.703	2003.026	105.0	39	52862.769	2003.609	281.0
17	52672.40928	2003.088	105.0	40	52865.680	2003.617	280.0
18	52679.32437	2003.107	105.0	41	52868.706	2003.625	280.0
19	52681.9927	2003.114	105.0	42	52871.751	2003.634	280.0
20	52682.00362	2003.114	105.0	43	52874.842	2003.642	280.0
21	52683.12669	2003.117	105.0	44	53007.240	2004.005	106.0
22	52686.35236	2003.126	105.0	45	53010.264	2004.013	105.0
23	52688.32956	2003.132	105.0	46	53014.107	2004.024	105.0

<sup>a</sup>MJD = JD - 2400000.5

<sup>b</sup>Spacecraft roll as defined in Chapter 2, FGS Instrument Handbook  
Nelán *et al.* (2003)

Table 2. Log of  $\epsilon$  Eri MAP Observations

Epoch	MJD <sup>a</sup>	Year	Epoch	MJD	Year
1	47544.0781	1989.0474	66	53001.0760	2003.988
2	47772.4045	1989.6726	67	50362.2622	1996.763
3	47790.3559	1989.7217	68	50362.2948	1996.763
4	47822.2920	1989.8091	69	50362.3281	1996.763
5	47826.2622	1989.8200	70	50371.2538	1996.788
6	47829.2503	1989.8282	71	50371.2872	1996.788
7	47905.0385	1990.0357	72	50371.3184	1996.788
8	47923.0024	1990.0849	73	50719.3260	1997.741
9	47933.0142	1990.1123	74	50719.3594	1997.741
10	48209.2163	1990.8685	75	50736.3129	1997.787
11	48213.2052	1990.8794	76	50736.3448	1997.787
12	48234.1406	1990.9367	77	50741.3281	1997.801
13	48281.0559	1991.0652	78	50798.1108	1997.956
14	48290.0135	1991.0897	79	50799.1316	1997.959
15	48528.3413	1991.7422	80	50799.1649	1997.959
16	48547.2948	1991.7941	81	51079.3615	1998.727
17	48901.3066	1992.7633	82	51079.3934	1998.727
18	48915.2816	1992.8016	83	51079.4253	1998.727
19	49007.9990	1993.0554	84	51100.3219	1998.784
20	49022.0066	1993.0938	85	51100.3538	1998.784
21	49027.0066	1993.1075	86	51145.1372	1998.907
22	49268.2733	1993.7680	87	51145.1698	1998.907
23	49274.2691	1993.7844	88	51145.2024	1998.907
24	49285.2309	1993.8145	89	51209.0010	1999.081
25	49302.2240	1993.8610	90	51829.2788	2000.780
26	49312.1545	1993.8882	91	51829.3115	2000.780
27	49334.1448	1993.9484	92	51829.3434	2000.780
28	49372.9997	1994.0548	93	52183.3115	2001.749
29	49597.4087	1994.6692	94	52183.3448	2001.749
30	49600.4003	1994.6773	95	52185.2774	2001.754
31	49640.3052	1994.7866	96	52219.1969	2001.847

Table 2—Continued

Epoch	MJD <sup>a</sup>	Year	Epoch	MJD	Year
32	49653.2205	1994.8220	97	52219.2316	2001.847
33	49668.1733	1994.8629	98	52219.2628	2001.847
34	49708.0587	1994.9721	99	52219.3080	2001.848
35	49747.0052	1995.0787	100	52219.3413	2001.8476
36	49748.0476	1995.0816	101	52220.2115	2001.8500
37	50362.2622	1996.7632	102	52220.2455	2001.8501
38	50371.2538	1996.7878	103	52225.1816	2001.8636
39	50719.3260	1997.7408	104	52225.2149	2001.8637
40	50736.3129	1997.7873	105	52225.2483	2001.8638
41	50741.3281	1997.8010	106	52226.1899	2001.8664
42	50798.1108	1997.9565	107	52226.2233	2001.8665
43	50799.1316	1997.9593	108	52226.2573	2001.8665
44	51079.3615	1998.7265	109	52227.2226	2001.8692
45	51100.3219	1998.7839	110	52227.2552	2001.8693
46	51145.1372	1998.9066	111	52265.0691	2001.9728
47	51209.0010	1999.0815	112	52265.1024	2001.9729
48	51829.2788	2000.7797	113	52265.1351	2001.9730
49	52183.3115	2001.7490	114	52893.3497	2003.6929
50	52185.2774	2001.7544	115	52893.383	2003.6930
51	52219.1969	2001.8472	116	52924.2726	2003.7776
52	52219.3080	2001.8475	117	52924.3059	2003.7777
53	52220.2115	2001.8500	118	52925.2747	2003.7804
54	52225.1816	2001.8636	119	52925.3094	2003.7805
55	52226.1899	2001.8664	120	52925.342	2003.7805
56	52226.2573	2001.8665	121	52925.3774	2003.7806
57	52227.2226	2001.8692	122	52937.2087	2003.8130
58	52265.0691	2001.9728	123	52937.2413	2003.8131
59	52893.3497	2003.6929	124	52946.224	2003.8377
60	52924.2726	2003.7776	125	52946.2566	2003.8378
61	52925.2747	2003.7804	126	52946.2899	2003.8379
62	52925.3420	2003.7805	127	53000.058	2003.9851

Table 2—Continued

Epoch	MJD <sup>a</sup>	Year	Epoch	MJD	Year
63	52937.2087	2003.8130	128	53001.076	2003.9879
64	52946.2240	2003.8377	129	53001.1177	2003.9880
65	53000.0580	2003.9851	130	53001.1448	2003.9881

<sup>a</sup>MJD = JD - 2400000.5

Table 3. The Radial Velocity Data Sets

Data Set	Coverage (yr)	Technique	N	RMS (m s <sup>-1</sup> )
CFHT	1980.81-1991.88	HF cell	48	10.5
Lick	1987.69-1998.99	Iodine cell	54	11.5
McD $\phi$ I	1988.74-1994.81	Telluric	27	15.2
McD $\phi$ II	1990.78-1998.07	Iodine cell	42	11.7
ESO	1992.84-1998.02	Iodine cell	36	9.6
McD $\phi$ III	1998.69-2004.86	Iodine cell	28	7.4
total			235	

Table 4. New McDonald  $\phi$ III Radial Velocities

mJD	RV <sub><math>\phi</math>III</sub> (m s <sup>-1</sup> )	mJD	RV <sub><math>\phi</math>III</sub> (m s <sup>-1</sup> )
51066.4339	-3.6±13.7	52539.4226	-16.4±14.3
51212.1671	13.6 13.4	52576.4378	2.0 13.7
51239.1133	1.7 14.1	52661.1445	-11.8 13.8
51449.4333	6.5 15.2	52931.3912	-13.9 14.8
51503.3574	14.7 14.1	52958.2449	-0.4 14.2
51529.1986	-3.5 13.8	52958.2481	0.0 14.1
51555.1645	-0.2 13.8	53016.2424	2.9 14.7
51775.4643	1.3 13.9	53016.2456	2.1 14.4
51809.4033	-2.7 14.1	53035.1757	-5.2 13.6
51917.2260	2.9 15.2	53075.0940	3.0 14.5
51984.0740	-2.8 14.2	53318.3124	-10.1 14.9
52142.4227	-0.7 14.6	53632.4520	-1.2 14.6
52142.4264	-0.4 14.3	53632.4550	0.4 14.3
52248.2921	-14.0 13.9	53689.3900	-3.0 13.7
52303.1266	-16.1 16.2	53745.2110	6.3 14.0
52328.1208	2.1 14.2	53809.0850	9.0 14.2
52330.1064	-0.9 14.1		

Table 5. FGS1r and MAP Astrometric Reference Stars

ID	Catalog	RA <sup>a</sup> (2000.0)	Dec <sup>a</sup>	V <sup>b</sup>	2MASS
1	ε Eri	53.232961	-9.458295	3.82	03325591-0927298
2		53.325845	-9.467569	15.61	03331820-0928032
3		53.312638	-9.434314	15.58	03331503-0926035
4		53.295306	-9.421752	16.12	03331087-0925183
5		53.269681	-9.418811	16.41	03330472-0925077
6		53.207917	-9.449667	16.48	
7	GEN# +6.10280864	53.374062	-9.504524	11.36	03332977-0930162
8	HD 22130	53.401866	-9.349848	9.52	03333644-0920594
9	BD-09 696	53.164328	-9.267778	10.69	03323943-0916040
10	GEN# +6.10280861	53.032108	-9.514245	11.60	03320770-0930512
11	BD-10 699	53.399013	-9.586081	10.24	03333576-0935098
12	HD 21951	53.001248	-9.385150	9.69	03320029-0923065
13	BD-10 695	53.320908	-9.696887	9.78	03331701-0941487
14	BD-10 700	53.466004	-9.641330	9.94	03335184-0938287
15	BD-09 699	53.429559	-9.232722	11.20	03334309-0913577
16	2MASS 03320556-0945292	53.023188	-9.758118	11.15	03320556-0945292

<sup>a</sup>Positions from 2MASS, except ID 6 from applying STScI Visual Target Tuner to the Digital Sky Survey.

<sup>b</sup>Magnitudes from FGS1r (ID 2-6), SIMBAD (ID 1), or MAP (ID 7- 16).

Table 6. V and Near-IR Photometry

ID	$V$	$K$	$(J - H)$	$(J - K)$	$(V - K)$
1	$3.82 \pm 0.01$	$1.82 \pm 0.05$	$0.40 \pm 0.28$	$0.48 \pm 0.07$	$2.00 \pm 0.05$
2	$15.61 \pm 0.03$	$13.01 \pm 0.03$	$0.58 \pm 0.04$	$0.72 \pm 0.04$	$2.60 \pm 0.04$
3	$15.58 \pm 0.03$	$14.09 \pm 0.06$	$0.41 \pm 0.05$	$0.44 \pm 0.07$	$1.50 \pm 0.06$
4	$16.12 \pm 0.03$	$13.88 \pm 0.05$	$0.51 \pm 0.04$	$0.59 \pm 0.06$	$2.24 \pm 0.06$
5	$16.41 \pm 0.03$	$14.21 \pm 0.08$	$0.46 \pm 0.07$	$0.62 \pm 0.09$	$2.20 \pm 0.08$
6	16.48				
7	$11.36 \pm 0.03$	$9.93 \pm 0.02$	$0.29 \pm 0.03$	$0.33 \pm 0.03$	$1.43 \pm 0.04$
8	$9.52 \pm 0.01$	$8.63 \pm 0.02$	$0.21 \pm 0.06$	$0.24 \pm 0.03$	$0.89 \pm 0.02$
9	$10.69 \pm 0.03$	$8.85 \pm 0.02$	$0.48 \pm 0.04$	$0.54 \pm 0.03$	$1.84 \pm 0.04$
10	$11.60 \pm 0.03$	$10.43 \pm 0.02$	$0.33 \pm 0.03$	$0.41 \pm 0.03$	$1.17 \pm 0.04$
11	$10.24 \pm 0.03$	$8.73 \pm 0.02$	$0.40 \pm 0.06$	$0.43 \pm 0.04$	$1.51 \pm 0.04$
12	$9.69 \pm 0.03$	$8.98 \pm 0.02$	$0.13 \pm 0.03$	$0.18 \pm 0.03$	$0.71 \pm 0.04$
13	$9.78 \pm 0.01$	$7.87 \pm 0.02$	$0.47 \pm 0.03$	$0.55 \pm 0.02$	$1.91 \pm 0.02$
14	$9.94 \pm 0.03$	$7.69 \pm 0.03$	$0.57 \pm 0.06$	$0.66 \pm 0.04$	$2.25 \pm 0.04$
15	$11.20 \pm 0.03$	$8.13 \pm 0.03$	$0.62 \pm 0.05$	$0.74 \pm 0.03$	$3.07 \pm 0.04$
16	$11.15 \pm 0.03$	$9.43 \pm 0.02$	$0.45 \pm 0.03$	$0.49 \pm 0.03$	$1.72 \pm 0.04$

Table 7. Astrometric Reference Star Adopted Spectrophotometric Parallaxes

ID	Sp. T. <sup>a</sup>	V	M <sub>V</sub>	m-M	$\pi_{abs}$ (mas)
2	K4V	15.6	7.1	8.5±1	1.9±1.0
3	G8V	15.6	5.6	10.0±0.4	1.0±0.2
4	K2V	16.1	6.5	9.6±0.4	1.2±0.2
5	K2V	16.4	6.5	9.9±0.4	1.0±0.2
6	K2V	16.4	6.5	9.9±2	1.0±0.9
7	G0V	11.4	4.4	7.0±0.4	4.1±0.7
8	F5V	9.5	3.5	6.0±0.4	6.3±1.2
9	K0V	10.7	5.9	4.8±0.4	11.0±2.0
10	G5V	11.6	5.1	6.5±0.4	5.0±0.9
11	G8V	10.2	5.6	4.6±0.4	11.8±2.2
12	F0V	9.7	2.7	7.0±0.4	4.0±0.7
13	K0V	9.8	5.9	3.9±0.4	16.7±3.1
14	K0III	9.9	0.7	9.2±0.4	1.4±0.3
15	K2III	11.2	2.7	8.5±0.4	2.0±0.4
16	G8V	11.2	5.6	5.6±0.4	7.8±1.4

<sup>a</sup>Spectral types and luminosity class estimated from colors and reduced proper motion diagram.

Table 8.  $\epsilon$  Eri and Reference Star Relative Positions

ID	$V$	$\xi^a$	$\eta^a$
1 <sup>b</sup>	3.73	297.0383±0.0001	35.6893±0.0001
2	15.57	-25.6479±0.0002	126.1290±0.0001
3 <sup>c</sup>	15.57	0.0000±0.0002	0.0000±0.0002
4	16.09	52.8710±0.0003	-55.1822±0.0002
5	16.40	433.1267±0.0003	-20.0260±0.0003
6	16.37	140.6876±0.0004	-81.2800±0.0002
1 <sup>d</sup>	3.73	715.2729±0.0002	201.7543±0.0002
7	11.36	1214.0919±0.0013	35.0491±0.0014
8	9.52	1313.1141±0.0005	591.8986±0.0007
9	10.69	469.2508±0.0011	887.5650±0.0014
10 <sup>e</sup>	11.60	0.0000±0.0021	0.0000±0.0025
11	10.24	1302.5205±0.0007	-258.4640±0.0011
12	9.69	-109.9029±0.0008	464.7282±0.0008
13	9.78	1025.1161±0.0005	-657.0894±0.0007
14	9.94	1540.2424±0.0005	-457.4732±0.0006
15	11.2	1411.6967±0.0011	1013.5480±0.0018
16	11.15	-31.1988±0.0015	-877.8886±0.0023

<sup>a</sup> $\xi$  and  $\eta$  are relative positions in arcseconds

<sup>b</sup>epoch 2002.614, J2000

<sup>c</sup>RA = 53.312638, Dec = -9.434314, J2000

<sup>d</sup>epoch 1996.761, J2000

<sup>e</sup>RA = 53.032108, Dec = -9.514245, J2000

Table 9. Reference Star Proper Motions

ID	V	Input (UCAC2)		Final ( <i>HST</i> )	
		$\mu_\alpha^a$	$\mu_\delta^a$	$\mu_\alpha^a$	$\mu_\delta^a$
2	15.57	0.0053±0.0078	-0.0112±0.008	0.0110±0.0002	- 0.0076±0.0002
3	15.57	0.0166±0.0076	-0.0014±0.0076	0.0072±0.0003	- 0.0026±0.0002
4	16.09	0.0044±0.009	-0.0028±0.0079	0.0080±0.0004	- 0.0022±0.0002
5	16.4	-0.0004±0.004	-0.0044±0.004	0.0070±0.0004	0.0082±0.0002
6	16.37	0.0064±0.003	0.0083±0.003	0.0014±0.0004	-0.0030±0. 0003
7	11.36	0.0253±0.005	0.0117±0.005	0.0221±0.0002	0.0083±0. 0003
8	9.52	0.0104±0.005	-0.0025±0.005	0.0088±0.0001	- 0.0052±0.0001
9	10.69	0.003±0.005	-0.0178±0.005	0.0035±0.0002	- 0.0184±0.0003
10	11.6	-0.0015±0.005	-0.0074±0.005	-0.0020±0.0004	- 0.0029±0.0004
11	10.24	0.0101±0.005	-0.0094±0.005	0.0126±0.0001	- 0.0089±0.0002
12	9.69	0.0095±0.005	-0.0038±0.005	0.0109±0.0001	- 0.0074±0.0002
13	9.78	0.0549±0.005	-0.037±0.005	0.0579±0.0001	- 0.0326±0.0001
14	9.94	-0.0003±0.005	-0.0079±0.005	-0.0017±0.0001	- 0.0102±0.0001
15	11.2	0.0117±0.005	-0.0063±0.005	0.0108±0.0002	- 0.0042±0.0003
16	11.15	0.0073±0.005	-0.0136±0.005	0.0052±0.0003	- 0.0158±0.0004

<sup>a</sup> $\mu_\alpha$  and  $\mu_\delta$  are relative motions in arcsec yr<sup>-1</sup>

Table 10.  $\epsilon$  Eri Parallax and Proper Motion

Parameter	<i>HST</i>	MAP	Combined
Study duration	2.92 y	14.94 y	
number of observation sets	46	130	
reference star $\langle V \rangle$	16.0	10.2	12.2
reference star $\langle (B - V) \rangle$			0.9 <sup>a</sup>
Absolute Parallax <sup>b</sup>			$311.37 \pm 0.11$ mas
Relative Proper Motion			$976.54 \pm 0.1$ mas y <sup>-1</sup>
in pos. angle			$269^{\circ}0 \pm 0^{\circ}6$
<i>HIPPARCOS</i> Absolute Parallax			$310.74 \pm 0.85$ mas
<i>HIPPARCOS</i> Proper Motion			$976.52 \pm 1.9$ mas y <sup>-1</sup>
in pos. angle			$271^{\circ}1 \pm 3^{\circ}8$

<sup>a</sup>Estimated from *VJHK* photometry with  $A_V = 0.0$ .

<sup>b</sup>Value from modeling RV and *HST* and MAP astrometry simultaneously

Table 11. Orbital Elements of  $\epsilon$  Eri Perturbation Due to  $\epsilon$  Eri b

Parameter	Value
$\alpha_A$	$1.88 \pm 0.20$ mas
$\alpha_A \sin i$	$3.02\text{e-}3 \pm 0.32\text{e-}3$ AU
P	$2502 \pm 10$ d
P	$6.85 \pm 0.03$ yr
T <sub>0</sub>	$54207 \pm 7$ mJD
T <sub>0</sub>	$2007.29 \pm 0.02$ y
e	$0.702 \pm 0.039$
i	$30^{\circ}1 \pm 3^{\circ}8$
$\Omega$	$74^{\circ} \pm 7^{\circ}$
$\omega$	$47^{\circ} \pm 3^{\circ}$
$K_1$	$18.5 \pm 0.2$ m s <sup>-1</sup>
$M_*$	$0.83 \pm 0.05 M_{\odot}$

Table 12.  $\epsilon$  Eri b Parameters

Parameter	Value
$a$ (AU)	$3.39 \pm 0.36$
$\Omega'$	$254^\circ$
$\omega'$	$47^\circ$
Mass Function ( $M_\odot$ )	$5.9\text{e-}10 \pm 1.0\text{e-}10$
$M \sin i$ ( $M_{\text{JUP}}$ ) <sup>a</sup>	$0.78 \pm 0.08$
$M$ ( $M_{\text{JUP}}$ ) <sup>b</sup>	$1.55 \pm 0.22$
$M$ ( $M_{\text{JUP}}$ ) <sup>c</sup>	$1.55 \pm 0.24$

<sup>a</sup>derived from radial velocity alone

<sup>b</sup>derived from radial velocity and astrometry, using  $M \sin i / \sin i$

<sup>c</sup>derived from radial velocity and astrometry, using  $m_2^3 / (m_1 + m_2)^2 = a^3 / P^2$ ; includes host star mass uncertainty.



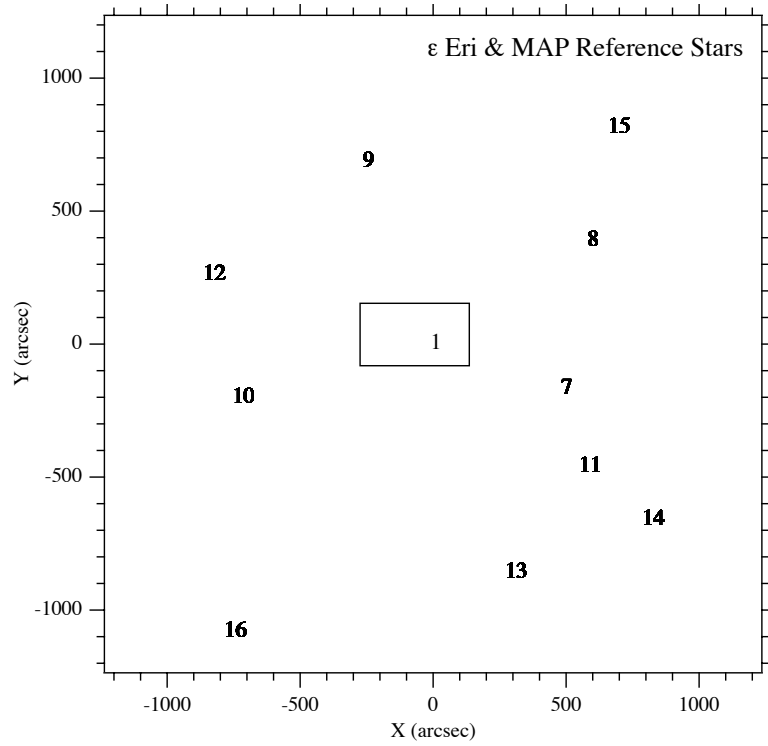


Fig. 1.—  $\epsilon$  Eri and MAP reference stars on the sky. Each star is identified by the number listed in Table 5. The inner box indicates the FGS1r reference frame coverage for epoch 2 in Table 1.

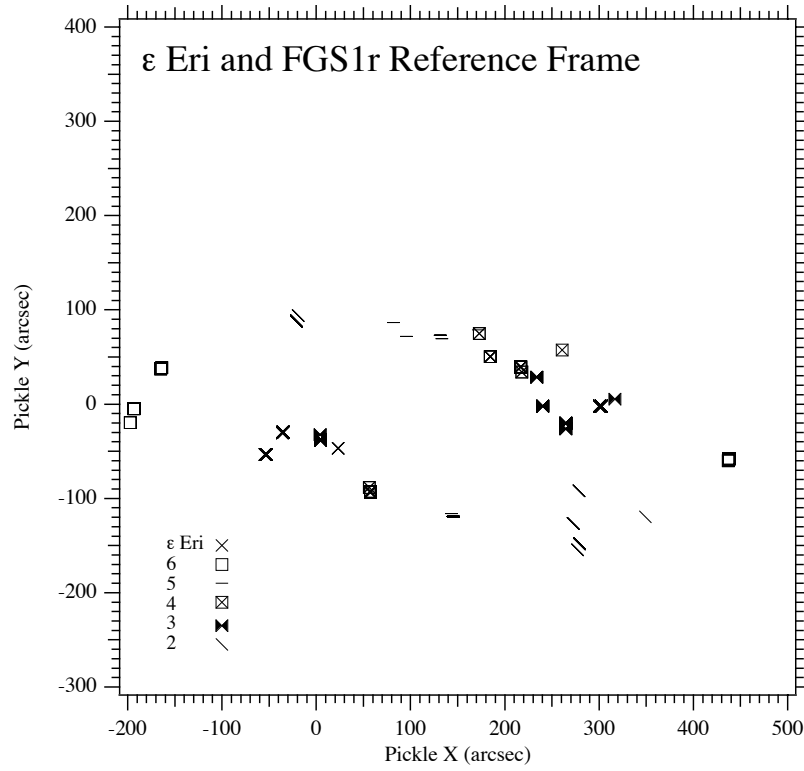


Fig. 2.— *HST*  $\epsilon$  Eri and reference frame observations in FGS1r pickle coordinates. The symbol shape identifies each star listed in Table 5. Note that the position of  $\epsilon$  Eri ( $\times$ ) within the FGS1r FOV is not fixed at the center.

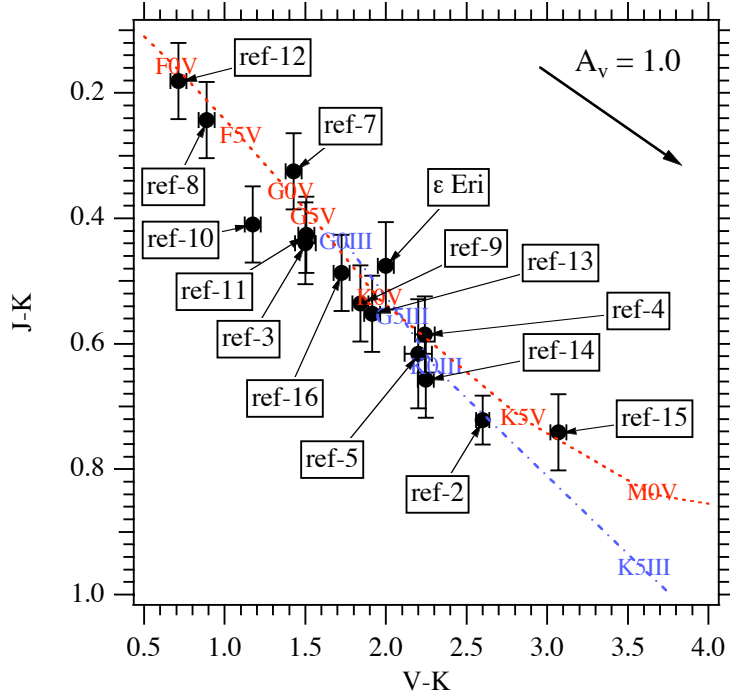


Fig. 3.—  $(J - K)$  vs.  $(V - K)$  color-color diagram for stars identified in Table 5. The dashed line is the locus of dwarf (luminosity class V) stars of various spectral types; the dot-dashed line is for giants (luminosity class III). The reddening vector indicates  $A_V = 1.0$  for the plotted color systems. Along this line of sight maximum extinction is  $A_V \sim 0.1$  (Schlegel *et al.* 1998).

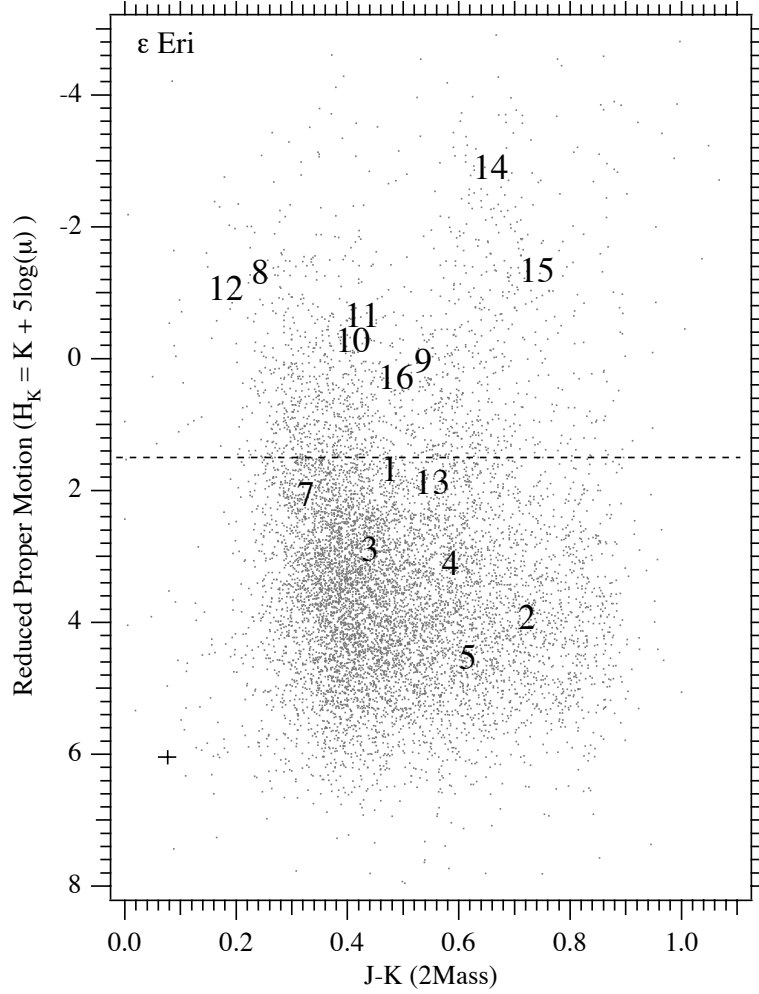


Fig. 4.— Reduced proper motion diagram for 9,041 stars in a  $6^\circ$  field centered on  $\epsilon$  Eri. Star identifications are in Table 5. For a given spectral type, giants and sub-giants have more negative  $H_K$  values and are redder than dwarfs in  $(J - K)$ .  $H_K$  values are derived from ‘Final’ proper motions in Table 9. The small cross at the lower left represents a typical  $(J - K)$  error of 0.04 mag and  $H_K$  error of 0.17 mag. The horizontal dashed line is a giant-dwarf demarcation derived from a statistical analysis of the Tycho input catalog (Ciardi 2004, private communication). Ref-14 and -15 are likely luminosity class III.

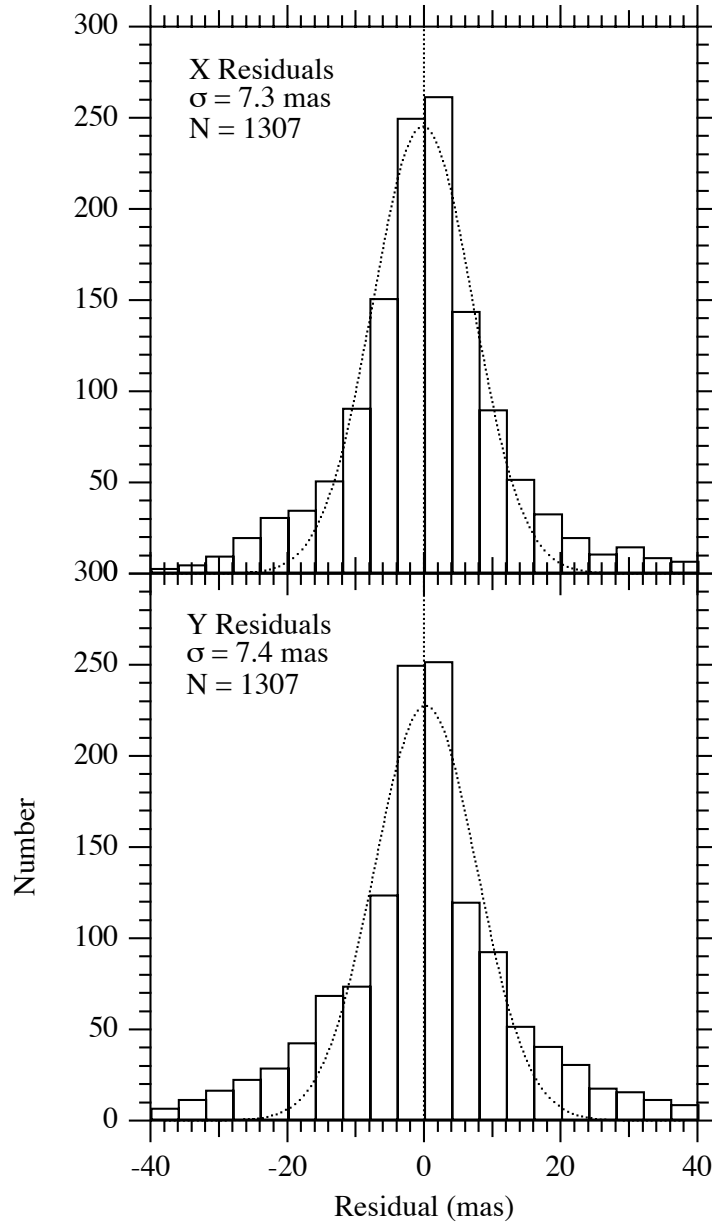


Fig. 5.— Histograms of x and y residuals obtained from modeling the MAP observations of  $\epsilon$  Eri and the MAP reference frame with equations 6 and 7. Distributions are fit with Gaussian distributions.

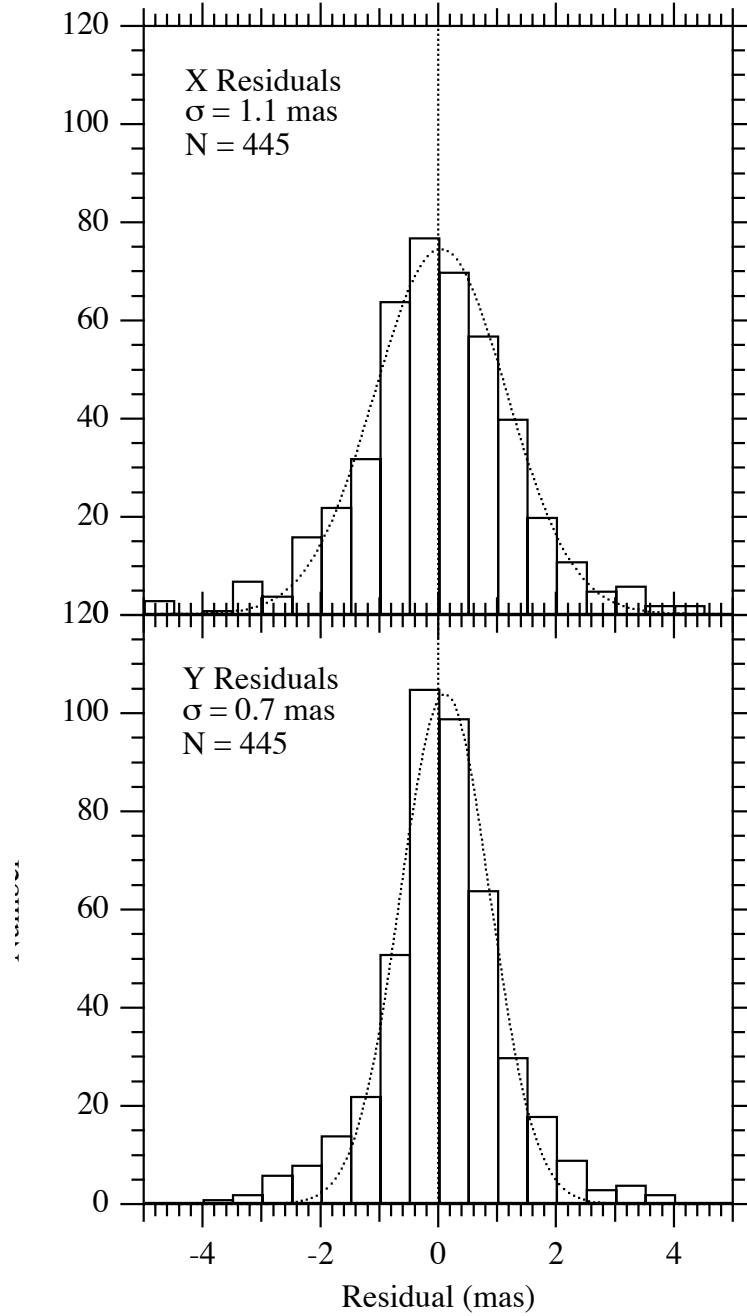


Fig. 6.— Histograms of x and y residuals obtained from modeling the FGS observations of  $\epsilon$  Eri and the FGS reference frame with equations 4 and 5. Distributions are fit with Gaussian distributions.



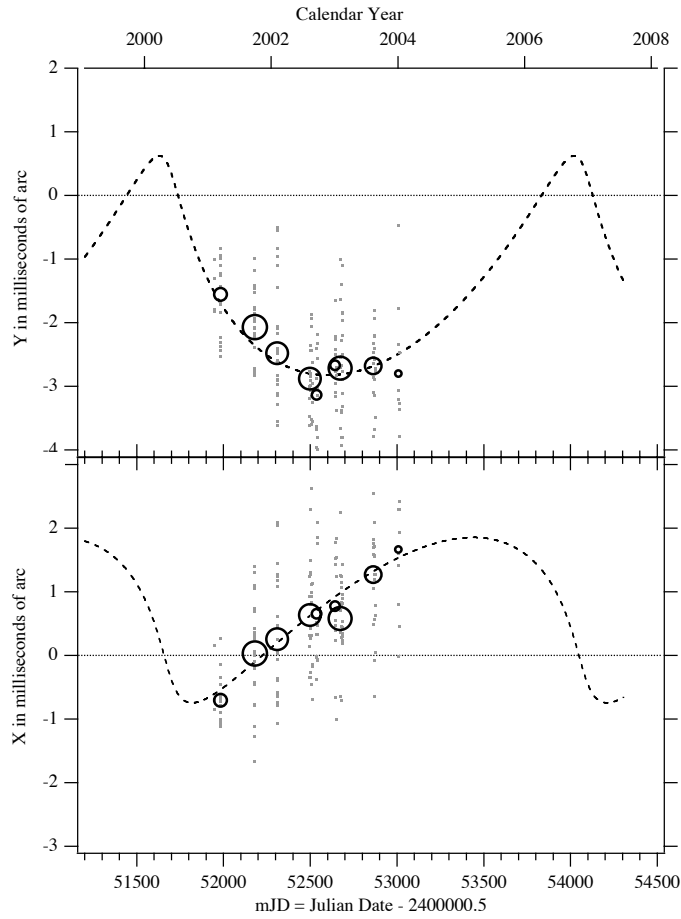


Fig. 7.— X and Y components of the perturbation orbit for  $\epsilon$  Eri as a function of time. The dashed line is the orbit described by the orbital elements found in Table 11. The dots are all the  $\epsilon$  Eri observation residuals to a model that does not contain orbital motion. The circles are normal points formed from the individual observation residuals, where the circle size is proportional to the number of observations forming the normal point.

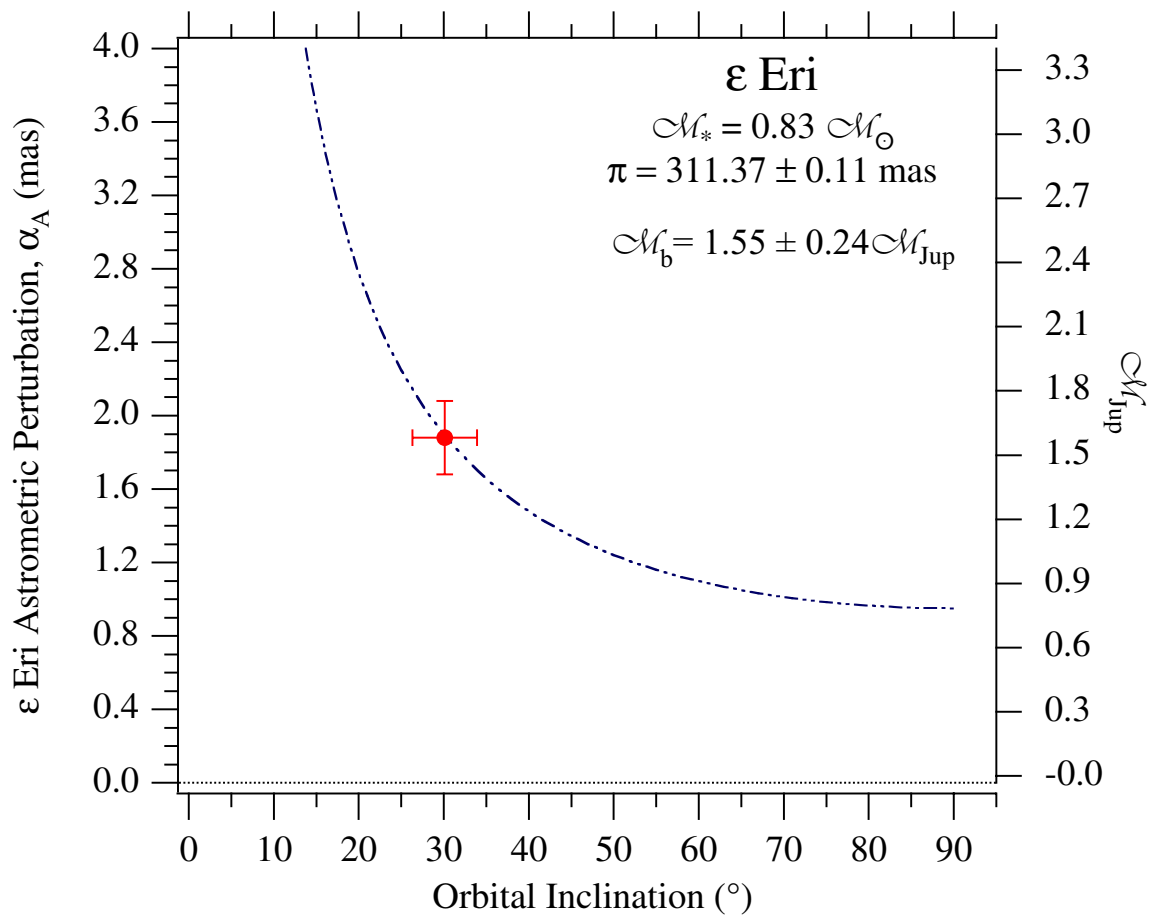


Fig. 8.— This curve relates perturbation size and inclination for the  $\epsilon$  Eri perturbation through the Pourbaix & Jorissen (2000) relation (Equation 10). We use the curve as a ‘prior’ in a quasi-Bayesian sense. Our final values for the semimajor axis of the astrometric perturbation,  $\alpha_A$ , and inclination,  $i$  are plotted with the formal errors.

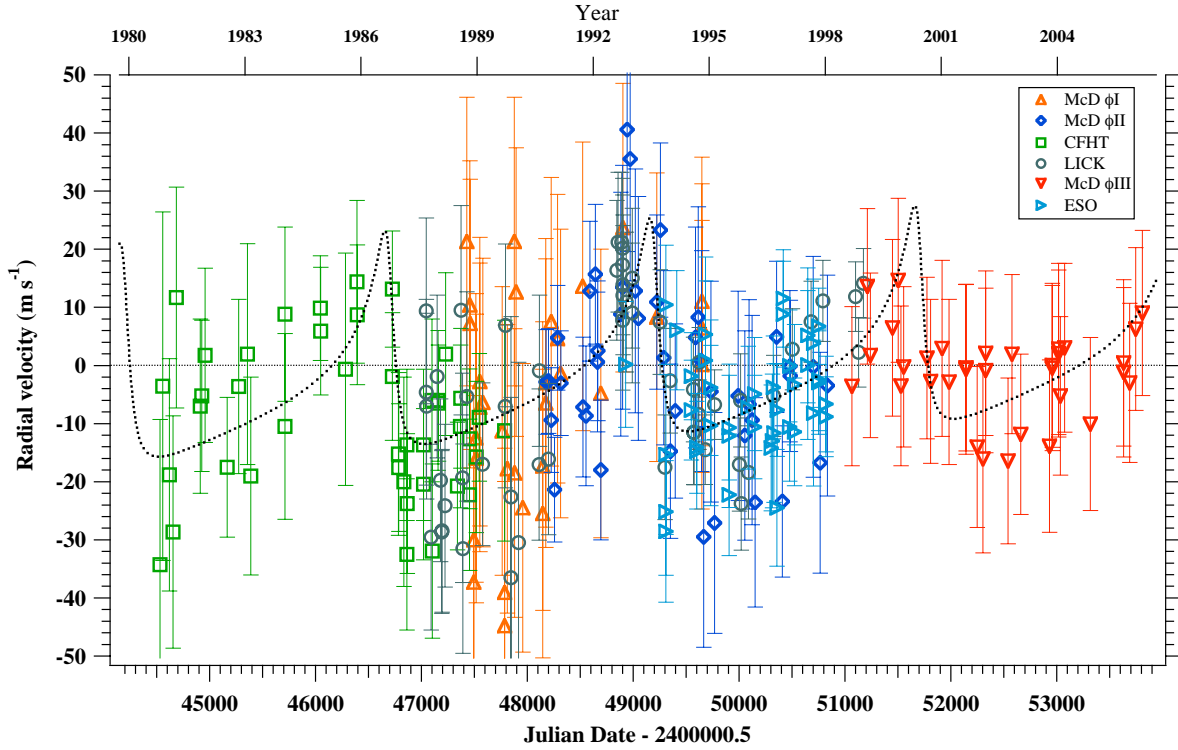


Fig. 9.— Radial velocity measurements of  $\epsilon$  Eri from sources as indicated in the legend (and identified in Table 3). The dashed line is the velocity predicted from the orbital parameters (Table 11) derived in the combined astrometry and radial velocity solution (Section 6). The linear trend in velocity can be seen by comparing the minima in the radial velocity orbit near 1981 with that at 2001.

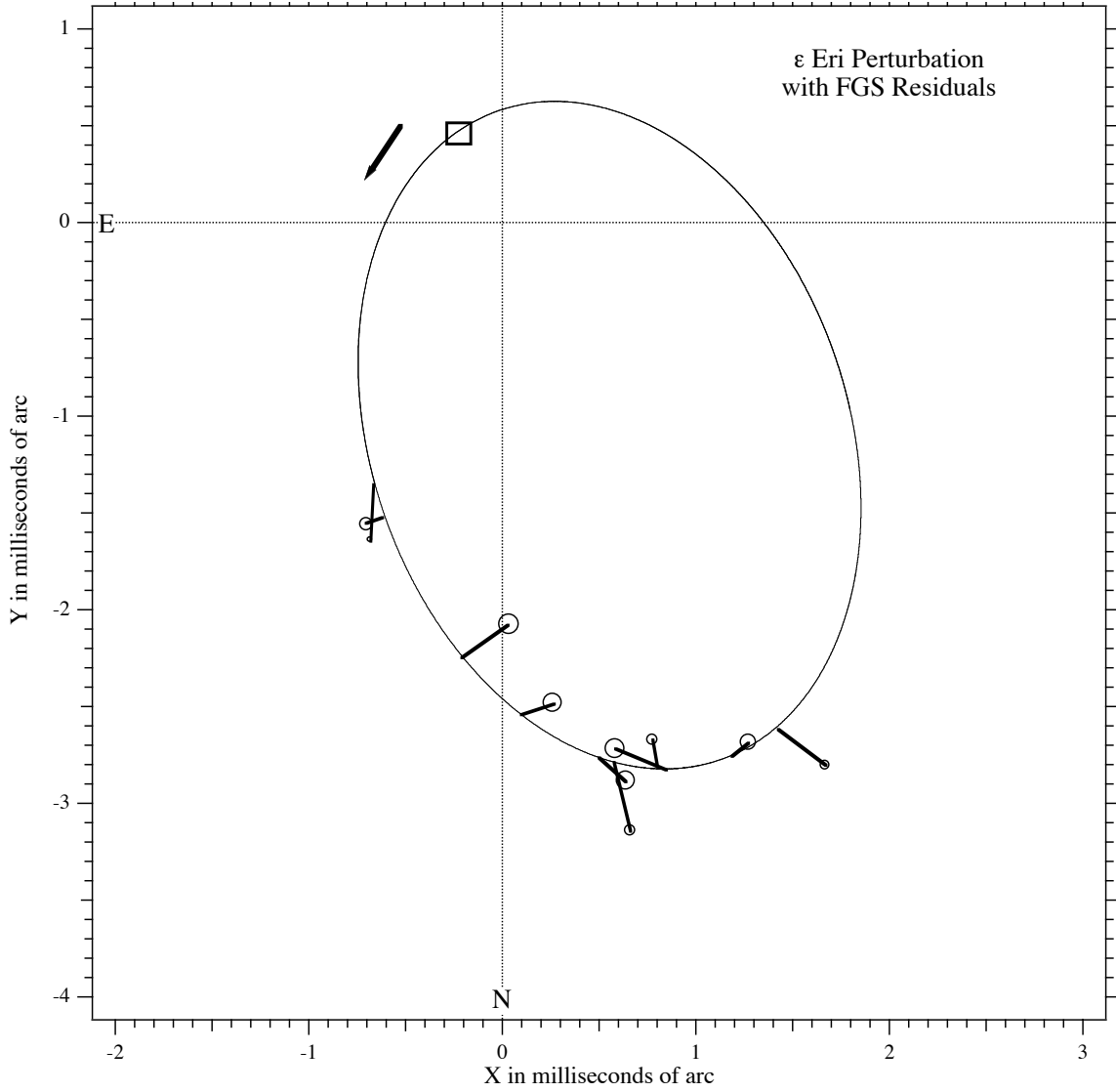


Fig. 10.— Perturbation orbit for  $\epsilon$  Eri. Elements are found in Table 11. Residual vectors are plotted, connecting each normal point residual to its predicted position at each epoch of observation. Circle size is proportional to the number of observations forming the normal point. The square marks periastron passage,  $T_0=2007.3$ . The arrow indicates the direction of motion of  $\epsilon$  Eri.